A Unit Protection Scheme Based on the Transient Current Coordinate Mapping Interval

Yao Sun, Yanfang Fan, Junjie Hou, and Guobing Song

***Abstract*—Modular multilevel converters (MMCs) have limited ability to withstand overcurrent. Additionally, the complex characteristics of faults make it extremely difficult to reliably identify the fault area within a short period. In this paper, the waveform of the transient current component is transformed into multiple intersecting curves in an alternative coordinate system, utilizing the principle of coordinate mapping. The internal and external faults are identified by determining the range of angles between the current waveforms and the time axis based on the intersecting regions of the curves. Subsequently, a unit protection scheme based on the transient current coordinate mapping interval is proposed. Finally, a modular multilevel converter-high voltage direct current (MMC-HVDC) system is built using PSCAD/EMTDC to validate the proposed scheme. The simulation results show that the proposed protection scheme is insensitive to factors such as current fluctuations caused by noise and distributed capacitive currents. In addition, it shows high robustness against fault resistance.**

***Index Terms*—Unit protection, MMC-HVDC, coordinate mapping, transient current waveform.**

I. Introduction

Modular multilevel converter (MMC) has the advantages of high output quality, low switching loss, and high scalability. Therefore, modular multilevel converter-high voltage direct current (MMC-HVDC) systems have been widely used in the fields of large-scale new energy aggregation, transmission, and grid interconnection [1]–[5]. However, the overhead lines used for long-distance transmission are susceptible to failures [5]. Moreover, the low damping of the DC system [6] and the nonlinear fault response characteristics of the converter lead to rapid fault development and complex characteristics. Therefore, a fast and reliable protection response is a prerequisite to ensure the safe and stable operation of the system, yet achieving this goal faces significant challenges.

Currently, the protection of DC lines can be categorized into non-unit protection [7]–[9] and unit protection according to whether they communicate. References [7] and [8] recognize the internal and external faults based on the boundary characteristics of the current-limiting reactors after the fault occurs. Reference [9] analyzes the transient high-frequency energy of the current to achieve fast identification of faults. Reference [10] uses wavelet transform to extract inputs for the artificial neural network algorithm, improving protection reliability to some degree. The above-mentioned methods are all non-unit protection schemes. They do not rely on communication and have advantages in terms of action speed. However, these methods face limitations such as the inability to reliably protect the entire transmission line, dependence on the boundaries, and limited sensitivity to high-resistance faults. Comparatively, unit protections offer higher reliability and sensitivity due to the use of more sampled data, and are selective in identifying faults.

The unit protections [11]–[25] can be divided into differential protections and pilot directional protections according to the type of communication data. Conventional current differential protections rely on directly measured currents to identify faults. However, these methods require a delay of several hundred milliseconds to avoid the effects of distributed capacitor current fluctuations. This delay slows down the entire protection system's response time [11]. Reference [12] improves the traditional differential protection by utilizing distributed optical sensors to enhance the speed of protection action. However, the method requires additional investment in equipment, and further study is needed to determine its actual engineering value. Reference [13] utilizes iterative calculations to eliminate the influence of distributed capacitance. However, this method increases the computational workload. References [14] and [15] utilize the similarity of transient surge current waveforms at both ends of the line to identify faults. Whereas these methods are easy to implement due to straightforward calculations, they require a large amount of sampling data. This dependence makes them

Received: January 6, 2024
Accepted: July 13, 2024
Published Online: January 1, 2025
Yao Sun, Yanfang Fan (corresponding author), and Junjie Hou (corresponding author) are with the School of Electrical Engineering, Xinjiang University, Urumqi 830000, China (e-mail: sy_sci@163.com; fyf_xj@sina.com; 826686025@qq.com).
Guobing Song is with the School of Electrical Engineering, Xi'an Jiaotong University, Xi'an 710000, China (e-mail: song.gb@mail.xjtu.edu.cn).
DOI: 10.23919/PCMP.2024.000010

susceptible to anomalous data and synchronization errors, which affects the speed and reliability of protection. Reference [16] analyzes the relationship between transmission line modeling and protection performance, and proposes a new current differential protection scheme. This scheme not only improves the protection speed but also enhances the sensitivity. The above-mentioned differential protection schemes are based on real-time communication of data at both ends of the line for fault identification. Most of these schemes require the setting of delays to mitigate the effects of distributed capacitance, making it challenging to meet the fast response requirements of MMC-HVDC system protection [17], [18]. The existing research on differential protection is mainly based on the traditional HVDC system. Therefore, there is a lack of well-established differential protection schemes for MMC-HVDC. In contrast to the differential protection scheme, the pilot directional protection [19]–[25] only communicates logic signals of the electrical quantities. Pilot directional protection offers several advantages including faster response times, reduced reliance on communication between stations, and the elimination of synchronization requirements. References [19] and [20] utilize the difference between the fault current components and the current traveling wave signs at both ends of the line to detect faults, respectively. These two schemes are simple in principle but unable to handle high resistance faults. Reference [21] analyzes the power extremes under different fault types in a modulus network for fault determination. However, the fault resistance capability of this method needs further discussion. To enhance the sensitivity of the protection scheme to high resistance faults, reference [22] proposes a unit protection scheme based on the impedance ratio of high and low frequencies at both ends of the line. Whereas this scheme exhibits a certain degree of noise resistance, the selection of the specific frequency band depends on the simulation. Reference [23] proposes a unit protection based on the characteristics of traveling wave refraction and reflection, utilizing the polarities of forward and backward traveling waves to enhance the capability of resisting high-resistance faults. Reference [24] proposes a unit protection scheme for comparing the direction of the initial voltage traveling wave transient energy at both ends of the line. However, this scheme requires a sampling frequency of 1 MHz. Reference [25] identifies faults based on the time difference between the arrival of forward and backward traveling waves. This approach avoids complex calculations, but its accuracy relies on the line boundaries and requires simulations to determine a threshold value.

In summary, the existing unit protection schemes still face several challenges: 1) Some unit protection schemes are susceptible to distributed capacitor current fluctuations, and have long action times [11], [13], making them unsuitable for long-distance MMC-HVDC systems; 2) Most of the existing pilot directional protection schemes are difficult to ensure reliability under high resistance faults [19]–[21]; 3) Some unit protection schemes are susceptible to anomalous data [14], [15], and the rectification values depend on simulation [22], [25]. The practicality of these schemes in real-world engineering projects needs further discussion.

To solve these challenges, this paper proposes a unit protection principle based on the transient current coordinate mapping interval. The contributions of this paper are as follows.

1) The proposed protection scheme utilizes the coordinate mapping principle to characterize the overall trend of transient current component waveforms. The proposed scheme is insensitive to anomalous data and fluctuations in distributed capacitive currents.

2) The proposed scheme utilizes the trend of the transient current to construct the differential characteristics of the internal and external faults, which does not involve specific calculations of the current amplitude and bending characteristics. Moreover, the proposed scheme is not affected by the fault resistance.

3) The proposed scheme does not require simulation to determine the threshold values.

The remaining parts of this article are arranged as follows. The coordinate mapping principle is presented in Section II and the differences between the current coordinate mapping intervals during internal and external faults are analyzed. The protection is presented in Section III. The key problems in the protection scheme are discussed in Section IV. The validity of the protection principle is verified by simulation in Section V. Finally, the conclusion is presented in Section VI.

II. Transient Current Coordinate Mapping Interval Analysis

Figure 1 illustrates a four-terminal MMC-HVDC system, which adopts a symmetrical bipolar structure. In the bipolar system, the pole-to-pole (PTP) fault of the DC line can be regarded as both the positive and negative poles experiencing a pole-to-ground (PTG) fault simultaneously. Therefore, this paper analyzes the transient current coordinate mapping intervals by taking the positive pole-to-ground (P-PTG) fault of Line1 as example. L_{dc} represents the current-limiting reactor, B12, B21, B13, and B24 are relays. MMC1#–MMC4# are converters, when # is ‘p’, they are positive converters, and when # is ‘n’, they are negative converters. Line1 is taken as the protection object, f1 represents an internal fault, f0 represents the backward external fault that occurs between the current-limiting reactor and MMC1, f01 and f21 represent the backward and forward external faults occurring on Line3 and Line2, respectively, and f2 represents the forward external fault that occurs between the current-limiting reactor and MMC2.

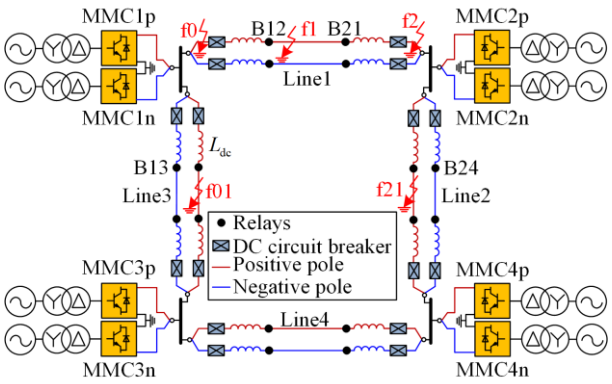

Fig. 1. Four-terminal MMC-HVDC system.

A. Transient Current Coordinate Mapping Interval Under Internal Faults

For MMC-HVDC, the transient process of a short-circuit fault can be divided into two stages: before the converter is blocked and after the converter is blocked. The proposed protection scheme utilizes the fault characteristics before the converter is blocked to identify internal and external faults. Therefore, the paper primarily focuses on the analysis of the stage before the converter is blocked. During a P-PTG, the fault current is mainly composed of the capacitor discharge current of the sub-modules (SMs). The equivalent circuit of the MMC during this stage is depicted in Fig. 2, where R_f is the fault resistance; L_0 and R_0 denote the inductance and resistance of the bridge arm, respectively; C_0 is the capacitance value of a single sub-module; and N_m is the number of sub-modules in a single-phase bridge arm.

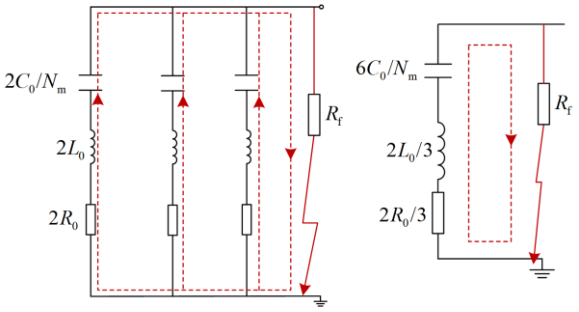

Fig. 2. Equivalent circuit before MMC converter blocking.

Before the converter is blocked, the equivalent impedance of the converter remains approximately constant. Consequently, based on the superposition theorem, Fig. 3 illustrates the fault component equivalent network for a P-PTG fault on Line1. At this point, it is equivalent to generating a negative voltage source u_f at the fault point. $R_{1,2}$, $L_{1,2}$, and $C_{1,2}$ represent the equivalent resistance, inductance, and capacitance of MMC1p and MMC2p, respectively, Z_{line3}, Z_{line2}, Z_{MMC3} and Z_{MMC4} are the equivalent impedances of Line3, Line2, MMC3p and MMC4p, respectively, while Δi_{B12} and Δi_{B21} are the transient current components measured by the relay at both ends of the positive line. The positive direction of the transient current component is assumed to be from the bus to the line. The positive direction of the negative line transient current component is from the line to the bus. The direction of the transient current component is determined by the combined effect of the additional power supply at the fault location and the prescribed positive direction.

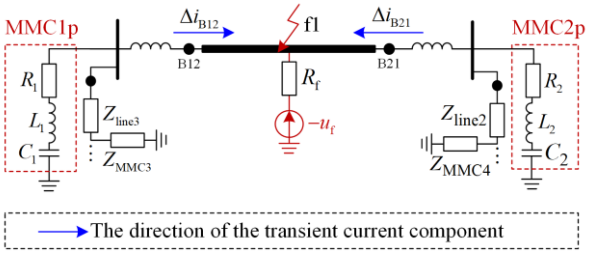

Fig. 3. Fault component equivalent circuit of internal fault.

In Fig. 3, the waveforms of the transient current component measured by B12 and B21 at the beginning of the fault show a rising trend. The current component waveform with a rising trend is represented by the curve Γ_{in} in Fig. 4(a). On this basis, the coordinate mapping intervals of transient currents during internal faults are analyzed.

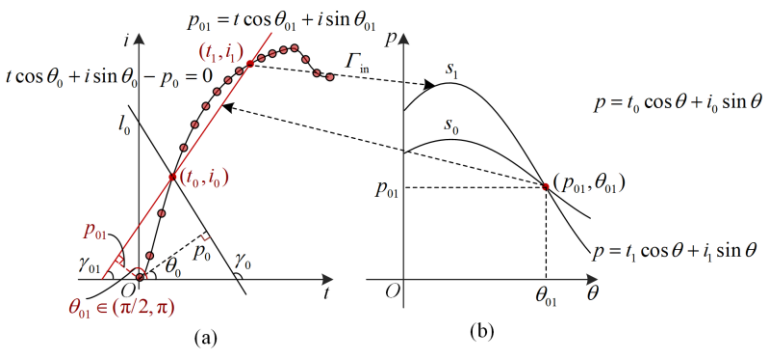

Fig. 4. Transient current coordinate mapping interval under internal fault. (a) The *t*-*i* coordinate system. (b) The θ-*p* coordinate system.

There are N sampling points set on Γ_{in}. (t_0,i_0) and (t_1,i_1) are any two points on Γ_{in}. The line l_0 passing over (t_0,i_0) is represented by its normal:

$$t\cos\theta_0 + i\sin\theta_0 - p_0 = 0 \tag{1}$$

where p_0 represents the distance from the origin to l_0; $\theta_0 \in (0,\pi)$ is the angle between the normal of l_0 and the horizontal axis.

At this point, the angle γ_0 between l_0 and the horizontal axis can be expressed by θ_0 as:

$$\gamma_0 = \begin{cases} \theta_0 + \dfrac{\pi}{2}, & 0 < \theta_0 \leqslant \dfrac{\pi}{2} \\ \theta_0 - \dfrac{\pi}{2}, & \dfrac{\pi}{2} < \theta_0 < \pi \end{cases} \tag{2}$$

Taking $t = t_0$ and $i = i_0$ as known quantities, θ as the independent variable, and p as the dependent variable, a curve s_0 in the θ-p coordinate system is:

$$p = t_0\cos\theta + i_0\sin\theta \tag{3}$$

For (t_1,i_1), any straight line l_1 passing through (t_1,i_1) can be represented by its normal as:

$$t\cos\theta_1 + i\sin\theta_1 - p_1 = 0 \tag{4}$$

Taking $t = t_1$, $i = i_1$ as known quantities, θ as the independent variable and p as the dependent variable, a curve s_1 in the θ-p coordinate system is:

$$p = t_1\cos\theta + i_1\sin\theta \tag{5}$$

The following relationship exists for the intersection (p_{01},θ_{01}) of curves s_0 and s_1:

$$t\cos\theta_{01} + i\sin\theta_{01} - p_{01} = 0 \tag{6}$$

The physical meaning of the line corresponding to (6) is the line passing through the two sampling points (t_0,i_0) and (t_1,i_1) in the t-i coordinates. $\pi/2 \pm \theta$ is the angle (γ_{01}) between this line and the horizontal axis. If $\gamma_{01} \in (0,\pi/2)$, then the corresponding line exhibits a rising trend, and if $\gamma_{01} \in (\pi/2,\pi]$, the line shows a falling trend. According to (2), if $\theta_{01} \in (\pi/2,\pi)$, then the corresponding straight line exhibits a rising trend, and if $\theta_{01} \in (0,\pi/2]$, the line shows a falling trend.

Through the above coordinate mapping method, in the fault current waveform (t-i coordinate system), all the sampling points are combined two by two according to the time order. $N(N-1)/2$ straight lines can be obtained in the t-i coordinate system, i.e., there are $N(N-1)/2$ intersections in the θ-p coordinate system. The denser the distribution of these intersection points, the closer the waveform is to a straight line. Therefore, θ is partitioned into n intervals, and the interval with the most intersections is defined as the transient current coordinate mapping interval, denoted by $\psi_{\max}$.

For internal faults, $\psi_{\max}$ of the transient current component at both ends of the faulted phase falls within the range of $(\pi/2,\pi)$.

B. Transient Current Coordinate Mapping Interval Under External Faults

Figure 5 shows the fault component network when a forward external fault occurs on the line.

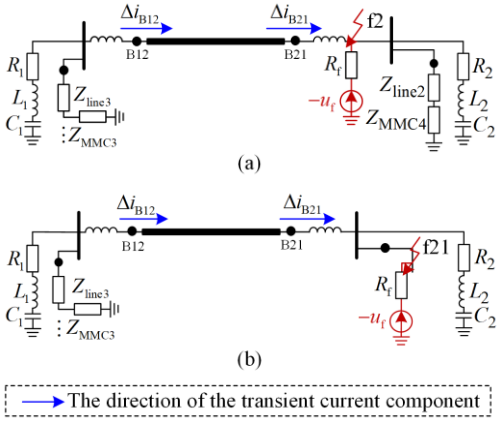

Fig. 5. Fault component equivalent circuit of forward external fault. (a) f2. (b) f21.

In Fig. 5, the transient current component measured by B12 shows a rising trend, while the component measured by B21 shows a falling trend. In Fig. 6(a), Γ_{12} and Γ_{21} represent current waveforms with rising and falling trends, respectively. (t_{10},i_{10}) and (t_{11},i_{11}) are any two sampling points on Γ_{12}, and (t_{20},i_{20}) and (t_{21},i_{21}) are any two sampling points on Γ_{21}, (p_1,θ_1) is the intersection point of the mapping of (t_{10},i_{10}) and (t_{11},i_{11}) in the θ-p coordinate system, (p_2,θ_2) is the intersection point of the mapping of (t_{20},i_{20}) and (t_{21},i_{21}) in the θ-p coordinate system.

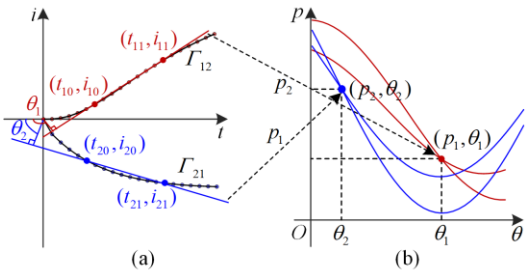

Fig. 6. Transient current coordinate mapping interval under external fault. (a) The t-i coordinate system. (b) The θ-p coordinate system.

When a forward external fault occurs, the current on one side of the protected line displays a rising trend with $\psi_{\max} \in (\pi/2,\pi)$, while the current on the other side shows a falling trend with $\psi_{\max} \in (0,\pi/2]$.

Figure 7 shows the fault component network when a backward external fault occurs on the line.

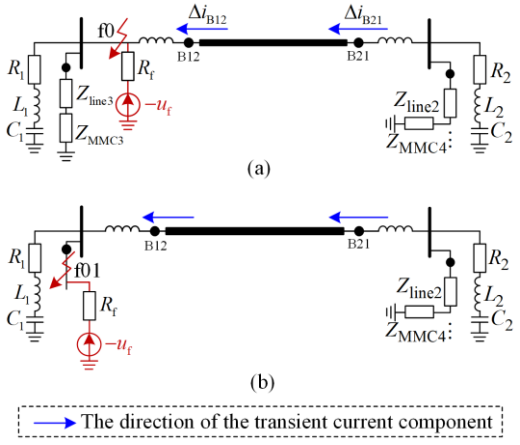

Fig. 7. Fault component equivalent circuit of backward external fault. (a) f0. (b) f01.

In Fig. 7, the transient current components measured by B12 and B21 show falling and rising trends, respectively. At this point, the current coordinate mapping relationship is similar to that of forward external faults.

In summary, when a backward external fault occurs, the current on one side of the protected line displays a rising trend with $\psi_{max} \in (\pi/2, \pi)$, while the current on the other side shows a falling trend with $\psi_{max} \in (0, \pi/2]$.

III. The Proposed Protection Scheme

A. Starting Criterion

The protection starting criterion is constructed using the fault current component:

$$|\Delta i_{\#}| > k_1 i_{dc} \tag{7}$$

where subscripts # being p and n represent the positive and negative pole respectively; $\Delta i_{\#}$ represents the amount of change in the current component; i_{dc} represents the current rating; k_1 represents the threshold coefficient, and in this paper $k_1 = 0.11$.

To ensure the anti-interference capability of the starting criterion, the system continuously evaluates three consecutive sampling points. If all three points satisfy (7), the protection is initiated. Additionally, to ensure data integrity, the sampling point before the first qualifying sampling point is taken as the initial point of the protection data window.

B. Fault Identification Criterion

From the analysis in Section II, the horizontal coordinates θ_c of the intersection of any two sampling points (t_m, i_m) and (t_n, i_n) in the current component waveform in the θ-p coordinate system are expressed as:

$$\theta_c = \begin{cases} \dfrac{\pi}{2}, & i_m = i_n \\ \arctan\left(\dfrac{t_n - t_m}{i_m - i_n}\right), & \dfrac{t_n - t_m}{i_m - i_n} > 0 \\ \pi + \arctan\left(\dfrac{t_n - t_m}{i_m - i_n}\right), & \dfrac{t_n - t_m}{i_m - i_n} < 0 \end{cases} \tag{8}$$

Equally dividing $\theta \in (0, \pi)$ into n intervals numbered $1, 2, 3, \cdots, n$ in the θ-p coordinate system, then the interval number $n_{\theta c}$ in which θ_c is located can be expressed as:

$$n_{\theta c} = \left\lceil \frac{\theta_c n}{\pi} \right\rceil \tag{9}$$

where $\lceil \ \rceil$ denotes rounding up.

The interval $\psi_{\theta c}$ in which θ_c lies is:

$$\psi_{\theta c} \in \begin{cases} \left(\dfrac{\pi}{n}(n_{\theta c} - 1), \dfrac{\pi}{n} n_{\theta c}\right], & n_{\theta c} < n \\ \left(\dfrac{\pi}{n}(n_{\theta c} - 1), \pi\right), & n_{\theta c} = n \end{cases} \tag{10}$$

The interval numbers where the horizontal coordinates of the intersection points of the remaining sampling points in the θ-p coordinate system are located can be calculated by (9) and (10). The interval number containing the highest number of intersection points is counted and the corresponding interval ψ_{max} is then determined.

In this paper, Q denotes the range of ψ_{max}:

$$Q = \begin{cases} -1, & \psi_{max} \in (0, \pi/2] \\ 1, & \psi_{max} \in (\pi/2, \pi) \end{cases} \tag{11}$$

To identify a fault, the protection identification criterion is constructed by summing Q at both ends of the line and compared against a threshold value of 1:

$$\begin{cases} Q_{B12\#} + Q_{B21\#} \geqslant 1, & \text{Internal fault} \\ Q_{B12\#} + Q_{B21\#} < 1, & \text{External fault} \end{cases} \tag{12}$$

where the subscripts 'B12' and 'B21' represent the sides B12 and B21, respectively.

According to the fault identification criteria, the protection operating interval is shown in Fig. 8(a).

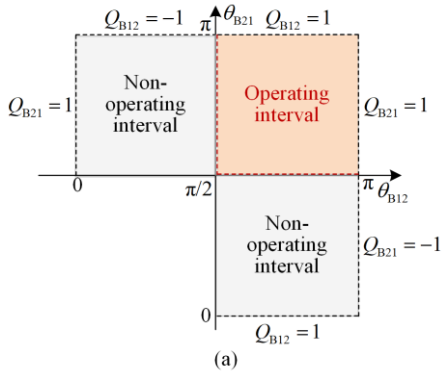

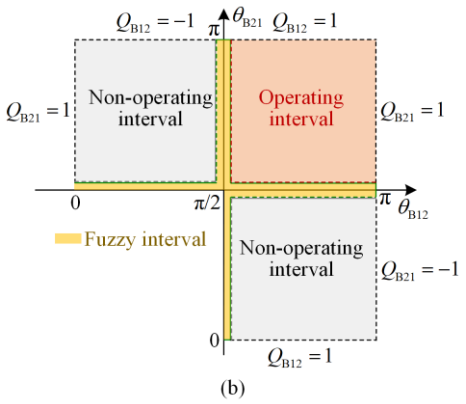

Fig. 8. Operating interval for protection. (a) Operating interval for protection before optimization. (b) Optimized protection operating interval.

In Fig. 8, the horizontal axis represents the angular interval $\theta_{B12} \in (0,\pi)$ corresponding to the current on side B12. The vertical axis represents the angular interval $\theta_{B21} \in (0,\pi)$ corresponding to the current on side B21.

We observe from Fig. 8 (a) that the critical value of the operating and non-operating intervals of the protection criterion is $\theta = \pi/2$. When θ equals to $\pi/2$ or is close to $\pi/2$ in a certain fault case, any intersection point (θ_r, p_r) whose horizontal coordinate falls within ψ_{max} can be substituted into (1):

$$t\cos\theta_r + i\sin\theta_r - p_r = 0 \tag{13}$$

Then, by assuming $\theta_r \approx \pi/2$, the following is obtained:

$$i \approx p_r \tag{14}$$

At this time, the current component waveform is shown in Fig. 9, where the direction of the arrows represents the order of coordinate mapping of the sampling points.

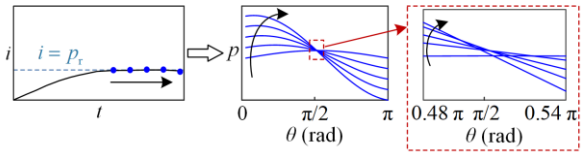

Fig. 9. Current coordinate mapping relationship for $\psi_{max} \approx \pi/2$.

The current component waveform can be approximated as a straight line parallel to the time axis, with $i = p_r$. This approximation makes it difficult to identify the range of ψ_{max} and may lead to a protection misjudgment. To enhance the reliability of the protection, this paper introduces the minimum range k to provide a certain margin to the action interval of the protection. It defines $(\pi/2-k, \pi/2+k]$ as the fuzzy interval in which $Q=0$ when ψ_{max} falls within the interval. The analysis of characteristics of the fault current shows that the farther away from the faults, the higher the fault resistance, the smoother the current waveform becomes. This means that in the event of internal or external high-resistance faults, the current component waveform on the line far from the fault point has the situation that ψ_{max} falls in the fuzzy interval. However, the current component waveform on the side close to the fault point still shows an obvious rising or falling trend. Thus, internal and external faults can be recognized according to the ψ_{max} on the side close to the fault point.

Based on the above analysis, the value of Q is updated to:

$$Q = \begin{cases} -1, \ \psi_{max} \in \left(0, \dfrac{\pi}{2}-k\right] \\ 0, \ \psi_{max} \in \left(\dfrac{\pi}{2}-k, \dfrac{\pi}{2}+k\right] \\ 1, \ \psi_{max} \in \left(\dfrac{\pi}{2}+k, \pi\right) \end{cases} \tag{15}$$

When an internal high-resistance fault occurs, the current component on the side of the line away from the fault point corresponds to $\psi_{max} \in (\pi/2-k, \pi/2+k]$, with $Q=0$. The current component on the side of the line close to the fault point corresponds to $\psi_{max} \in (\pi/2+k, \pi)$. The sum of the values of Q at both ends of the line equals 1. When an external high-resistance fault occurs, the current component on the side of the line away from the fault point corresponds to $\psi_{max} \in (\pi/2-k, \pi/2+k]$, with $Q=0$. The current component on the side of the line close to the fault point corresponds to $\psi_{max} \in (0, \pi/2-k]$. The sum of the Q at both ends of the line equals –1. The resulting optimized fault identification criterion is:

$$\begin{cases} Q_{B12\#} + Q_{B21\#} > 0, & \text{Internal fault} \\ Q_{B12\#} + Q_{B21\#} \leqslant 0, & \text{External fault} \end{cases} \tag{16}$$

The optimized protection operating interval is shown in Fig. 8(b).

The effect of the magnitude of k on the protection will be clarified next. If k is too large, ψ_{max} of the currents at both ends of a faulted line may fall within the fuzzy interval, leading to protection misjudgment. If k is too small, the concept of fuzzy interval becomes irrelevant. In this paper, k is set equal to the θ unit interval $\Delta\theta$ to reduce the computational effort of the protection algorithm. The analysis in Section II, the sparser the angular distribution corresponding to the intersection point in the θ-p coordinate system, the greater the fluctuation of the transient current component waveform. Therefore, the larger $\Delta\theta$, the greater the anti-interference capability of the protection. However, if $\Delta\theta$ is too large, the number of fluctuations of the current waveform will directly affect the identification result of the protection. Considering the anti-interference capability and sensitivity of the protection, $\Delta\theta$ in this paper is set to 5°, which is equal to $\pi/36$.

C. Fault Pole Criterion

When a PTG fault occurs, the current mapping intervals at both ends of the faulty pole line will be $\psi_{\max} \in (\pi/2+k, \pi)$, and the sum of Q will be greater than 0. The current mapping intervals at both ends of the non-faulty pole will be $\psi_{\max} \in (\pi/2+k, \pi)$ and $\psi_{\max} \in (0, \pi/2-k]$. Additionally, the sum of Q at both ends will be equal to 0.

When a PTP fault occurs, the current mapping intervals at both ends of the positive and negative lines will be $\psi_{\max} \in (\pi/2+k, \pi)$ and the sum of Q will be greater than 0.

Combining the fuzzy intervals, the fault pole criterion is thus obtained as:

$$\begin{cases} Q_{\mathrm{B12p}} + Q_{\mathrm{B21p}} > 0 \,\&\, Q_{\mathrm{B12n}} + Q_{\mathrm{B21n}} \leqslant 0, & \text{P-PTG fault} \\ Q_{\mathrm{B12n}} + Q_{\mathrm{B21n}} > 0 \,\&\, Q_{\mathrm{B12p}} + Q_{\mathrm{B21p}} \leqslant 0, & \text{N-PTG fault} \\ Q_{\mathrm{B12p}} + Q_{\mathrm{B21p}} > 0 \,\&\, Q_{\mathrm{B12n}} + Q_{\mathrm{B21n}} > 0, & \text{PTP fault} \end{cases} \tag{17}$$

D. Protection Scheme

Figure 10 shows the flow chart of the proposed protection scheme that combines the starting criterion, fault identification criterion and fault pole criterion. The protection scheme process is detailed as follows:

1) The measured current component is used as the 1starting criterion, and protection is initiated when the conditions are met.

2) Extract the current components on both sides of the fault line and calculate the intersection point of each sampling point in the θ-p coordinate system using (1)–(6).

3) Solve the interval number corresponding to the horizontal coordinate of the intersection point according to (9).

4) Calculate the interval range $\psi_{\max}$ corresponding to this number using (10), and determine Q according to $\psi_{\max}$.

5) To identify the fault, add up the Q corresponding to the currents at both ends and compare it with the threshold value.

6) Fault pole identification can be achieved separately using (17).

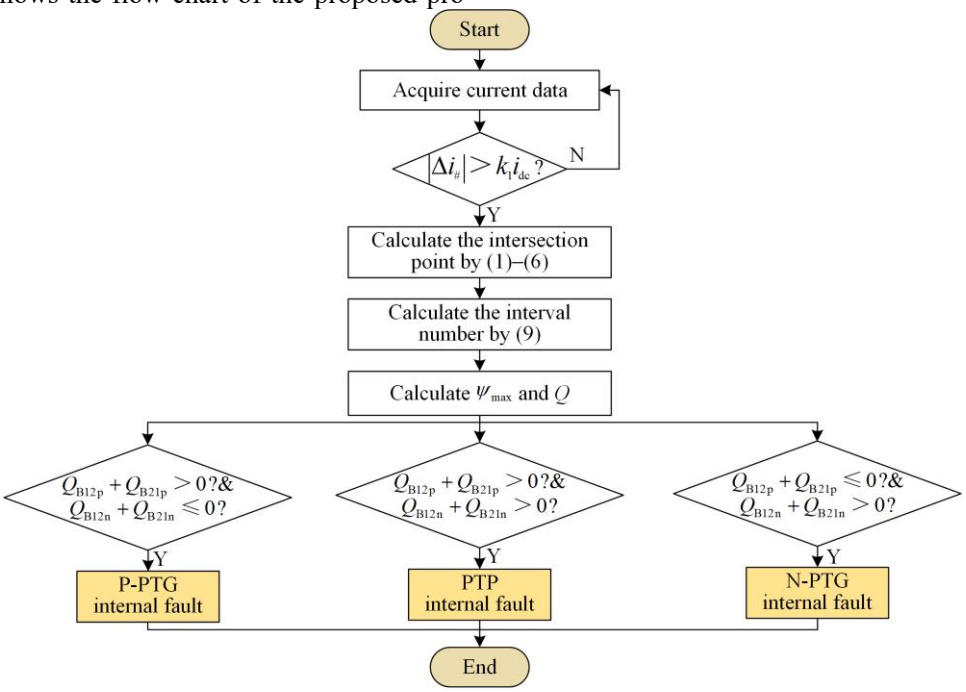

Fig. 10. Flow chart of the proposed protection scheme.

IV. Discussion of Relevant Problems

A. Discussion of Protection Identification Accuracy

The ability of the proposed protection scheme to accurately identify $\psi_{\max}$ directly influences the protection identification accuracy. Fault in HVDC systems develop very quickly, typically within milliseconds, the sampling frequencies are mostly in the range of 10 kHz to 100 kHz [7]–[10], [21], [25], [26], and fault currents are typically several kA.

If the time and current orders of magnitude significantly differ in the coordinate mapping, then:

$$\theta_{\mathrm{c}} \approx \begin{cases} 0, & \dfrac{t_{\mathrm{n}} - t_{\mathrm{m}}}{i_{\mathrm{m}} - i_{\mathrm{n}}} > 0 \,\&\, i_{\mathrm{m}} - i_{\mathrm{n}} \gg t_{\mathrm{n}} - t_{\mathrm{m}} \\ \dfrac{\pi}{2}, & |i_{\mathrm{m}} - i_{\mathrm{n}} \ll t_{\mathrm{n}} - t_{\mathrm{m}}| \\ \pi, & \dfrac{t_{\mathrm{n}} - t_{\mathrm{m}}}{i_{\mathrm{m}} - i_{\mathrm{n}}} < 0 \,\&\, i_{\mathrm{m}} - i_{\mathrm{n}} \gg t_{\mathrm{n}} - t_{\mathrm{m}} \end{cases} \tag{18}$$

To prevent the problem that all θ_{c} computed in the data window are concentrated around 0, π/2 and π,

which leads to low accuracy in the recognition of coordinate mapping intervals, θ_c dispersed in [π/36, 17π/36] and [19π/36, 35π/36] is a reasonable range. This can be obtained by combining (8):

$$\frac{\pi}{36} \leqslant \arctan\left(\left|\frac{t_n - t_m}{i_m - i_n}\right|\right) \leqslant \frac{17\pi}{36} \tag{19}$$

i.e.,

$$0.087 \leqslant \left|\frac{t_n - t_m}{i_m - i_n}\right| \leqslant 11.43 \tag{20}$$

Table I shows the difference between the horizontal and vertical coordinate orders of magnitude at different sampling frequencies.

TABLE I
DIFFERENCE BETWEEN HORIZONTAL AND VERTICAL COORDINATE ORDERS OF MAGNITUDE AT DIFFERENT SAMPLING FREQUENCIES

	10 kHz	20 kHz	50 kHz	100 kHz
$\lvert t_n - t_m \rvert$ (s)	10^{-4}	5×10^{-5}	2×10^{-5}	10^{-5}
$\lvert i_m - i_n \rvert$ (A)	10^{2}	5×10	2×10	10
$\lvert (t_n - t_m)/(i_m - i_n) \rvert$	**10^{-6}**	**10^{-6}**	**10^{-6}**	**10^{-6}**
$\lvert t_n - t_m \rvert$ (s)	10^{-4}	5×10^{-5}	2×10^{-5}	10^{-5}
$\lvert i_m - i_n \rvert$ (kA)	10^{-1}	5×10^{-2}	2×10^{-2}	10^{-2}
$\lvert (t_n - t_m)/(i_m - i_n) \rvert$	**10^{-3}**	**10^{-3}**	**10^{-3}**	**10^{-3}**
$\lvert t_n - t_m \rvert$ (μs)	10^{2}	5×10	2×10	10
$\lvert i_m - i_n \rvert$ (kA)	10^{-1}	5×10^{-2}	2×10^{-2}	10^{-2}
$\lvert (t_n - t_m)/(i_m - i_n) \rvert$	**10^{3}**	**10^{3}**	**10^{3}**	**10^{3}**
$\lvert t_n - t_m \rvert$ (ms)	10^{-1}	5×10^{-2}	2×10^{-2}	10^{-2}
$\lvert i_m - i_n \rvert$ (kA)	10^{-1}	5×10^{-2}	2×10^{-2}	10^{-2}
$\lvert (t_n - t_m)/(i_m - i_n) \rvert$	**1**	**1**	**1**	**1**

We observe that: 1) A change in the sampling rate does not alter the gap between the horizontal and vertical coordinates in the same axis unit. This is because the time interval in the horizontal coordinate is proportional to the current increment in the vertical coordinate, and a decrease in the time interval results in an exponentially smaller current increment; 2) The conditions of (20) are satisfied when the units of the horizontal and vertical coordinate axes are 'ms' and 'kA' respectively. Therefore, 'ms' and 'kA' are reasonable choices when the sampling rate is from 10 kHz to 100 kHz.

B. Processing of Data Window

The proposed protection scheme addresses the coordinate mapping interval of the initial trend feature of the transient current at the beginning of the fault. The change in the trend of the current will impact fault identification accuracy. Therefore, it is necessary to analyze the duration of the initial trend feature of the current for the time t_c, and then determine the length of the protection data window.

According to the theory of refraction and reflection of traveling waves, when an internal fault occurs, the current on the side away from the point of fault begins to fall at the moment when the transient voltage component is 0 after the arrival of the second travelling wave. The farther away from the fault and the higher the fault resistance is, the smaller t_c is. When t_c is the smallest, it is denoted by $t_{c\_in\_min}$.

When an external fault occurs, the moment of change in the current trend on the side close to the fault point coincides with the point of transient voltage drop minimization. The larger the fault resistance and the closer the fault is, the smaller t_c is. When t_c is smallest it is expressed by $t_{c\_out\_min}$ ($t_{c\_in\_min} > t_{c\_out\_min}$).

If the data window length is $t_{c\_in\_min}$, when an external fault occurs, the ψ_{max} calculated under this data window cannot characterize the initial trend of the transient current. If the data window length is $t_{c\_out\_min}$, the reliability of the protection may be affected due to the data window being too short, leading to protection misjudgment.

Therefore, this paper proposes segmented data window. Firstly, $t_{c\_in\_min}$ is taken as the length of the long data window, $t_{c\_in\_min}$ is segmented evenly, and the length of each small data window t_{ev} should be satisfied:

$$\begin{cases} t_{c\_out\_min} < t_{ev} < 2t_{c\_out\_min} \\ t_{ev} \leqslant t_{c\_in\_min} \end{cases} \tag{21}$$

If the Q calculated for each small data window within a long data window includes both 1 and −1, it indicates an external high resistance fault. The direction of the external fault can be determined from the Q calculated in the first small data window. If the Q values calculated for all small data windows are the same except for 0, the fault area can be identified by examining any data window where $Q \neq 0$.

C. Influence of Distributed Capacitance Current

The analysis in Section II shows that with the increase of lines, the transient current generated by the discharging process of the distributed capacitance becomes more significant after a fault occurs. Let C_{c1}, and C_{c2} are the distributed capacitances with transient voltages u_{c1} and u_{c2}, respectively, and i_{f12} is the current flowing to the fault point on the B12 side. At this time, the transient current component on the B12 side can be expressed as:

$$i_{B12} = i_{f12} - C_{c1}\frac{du_{c1}}{dt} - C_{c2}\frac{du_{c2}}{dt} \tag{22}$$

From (22), we observe that the distributed capacitor discharge leads to fluctuations in the transient current components at both ends of the line. However, these fluctuations do not alter the overall trend of the current waveform. The fault identification criterion proposed in

this paper is based on angular intervals, this indicates that γ can also be active in a certain interval, which improves the protection's anti-interference capability.

V. Simulation Analysis

The ±520 kV four-terminal MMC-HVDC model is built on PSCAD/EMTDC, as depicted in Fig. 1. The MMC converter, consisting of half-bridge SMs, does not have fault self-clearing capability. MMC1-MM3 adopt constant active power and reactive power control, and MMC4 adopts constant DC voltage and reactive power control. The detailed system parameters are listed in Table II. The DC line adopts a frequency-dependent parameter model. Figure 11 shows the line structure with a length of 400 km and L_{dc} being 150 mH at both ends of the line. The protection sampling frequency is 20 kHz. $t_{c\_in\_min}=1$ ms, and length of each small data window t_{ev} is 0.25 ms.

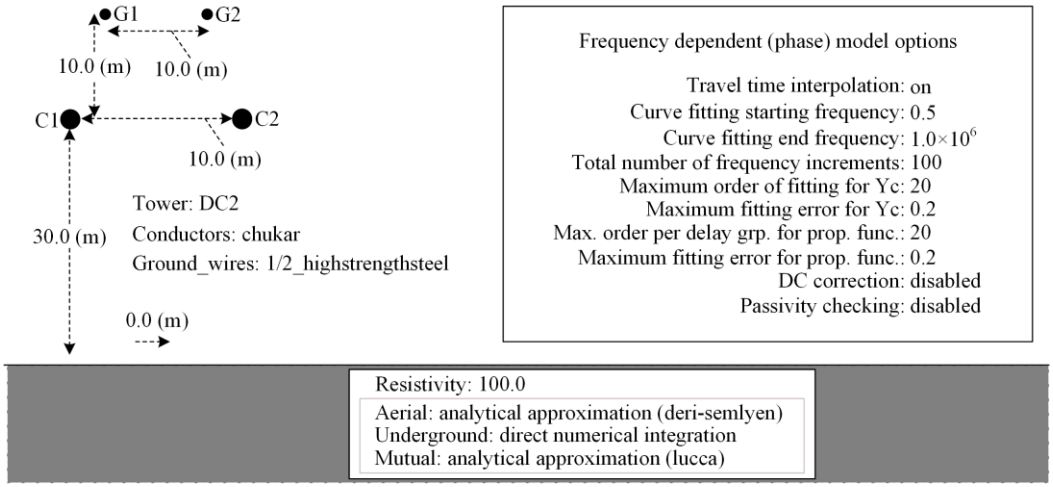

Fig. 11. Frequency-dependent overhead line model.

TABLE II
Parameters of MMC-HVDC System

Parameters	MMC1	MMC2	MMC3	MMC4
Rated capacity (MW)	1500	1500	1500	1500
Current-limiting reactor(mH)	150	150	150	150
SM capacitance (mF)	15	10	15	15
Number of arm SM	200	200	200	200
Arm reactor (mH)	100	100	50	50
Rated AC voltage (kV)	230	525	230	525
Rated DC voltage (kV)	±520	±520	±520	±520

A. Simulation Verification of Mapping Relations

B12 on Line1 is used as a study object to verify the correctness of the current mapping relations under different fault conditions.

1) Different Fault Locations

A P-PTG fault occurs at f0, f1 (midpoint of Line1), and f2 respectively. The fault resistance is set to 0.1 Ω. Figure 12 shows the mapping relation of Δi_{B12p}. Sub-figures 1), 2), 3), and 4) in Figs. 12(b) and (c) represent the 1st, 2nd, 3rd, and 4th data windows, respectively. Table III lists $\psi_{B12p,max}$ derived for different fault locations in Fig. 12(c).

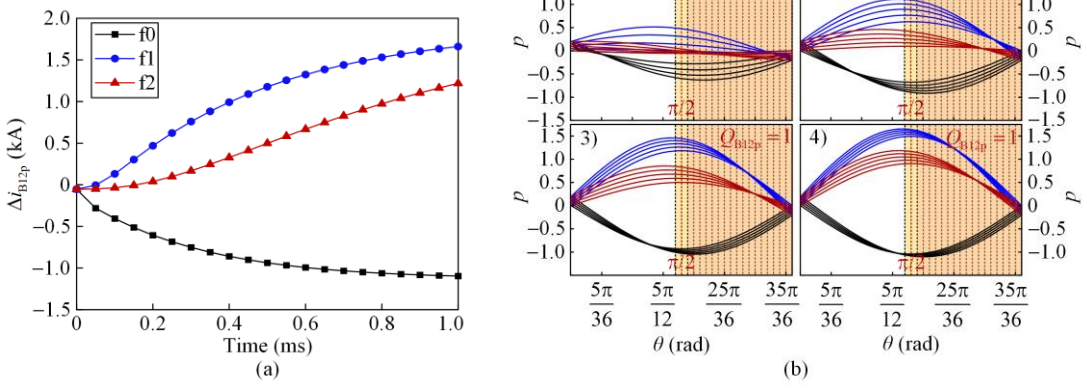

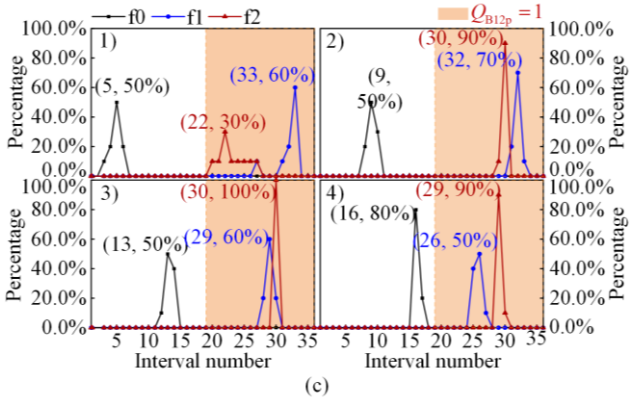

Fig. 12. Mapping relationships of current waveforms at different fault locations. (a) Waveform of transient current. (b) Coordinate mapping relations of the current waveform. (c) Interval numbers of intersection distributions.

TABLE III
$\psi_{B12p,max}$ AT DIFFERENT FAULT LOCATIONS

Fault location	1) $\psi_{B12p,max}$	2) $\psi_{B12p,max}$	3) $\psi_{B12p,max}$	4) $\psi_{B12p,max}$
f0	(π/9, 5π/36]	(2π/9, π/4]	(π/3, 13π/36]	(5π/12, 4π/9]
f1	(8π/9, 11π/12]	(31π/36, 8π/9]	(7π/9, 29π/36]	(25π/36, 13π/18]
f2	(7π/12, 11π/18]	(29π/36, 5π/6]	(29π/36, 5π/6]	(7π/9, 29π/36]

2) Different Fault Resistances

A P-PTG fault occurs at f1 (midpoint of Line1). The fault resistance is set to be 0.1 Ω, 200 Ω, and 800 Ω, respectively. Figure 13 shows the mapping relationships of the waveforms of the positive line transient current components on the B12 side and Table IV shows the values $\psi_{B12p,max}$ derived for different fault resistances.

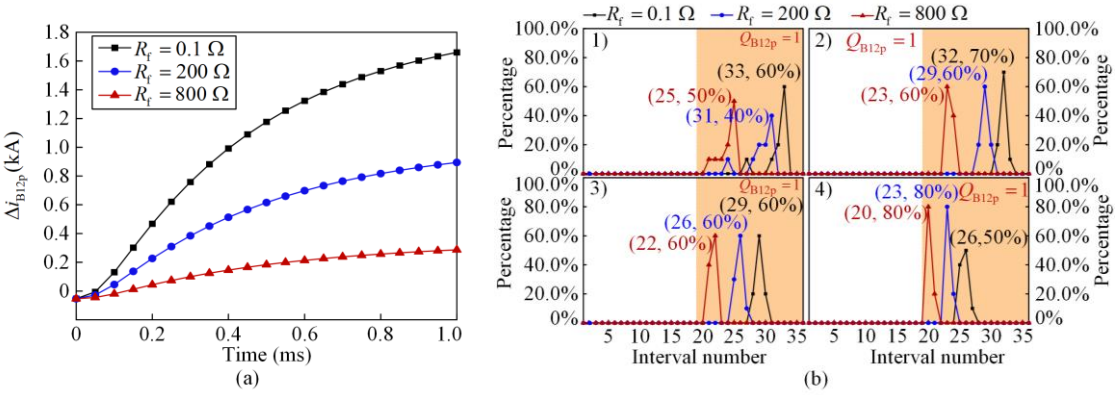

Fig. 13. Mapping relationships of current waveforms at different fault resistances. (a) Waveform of transient current. (b) Interval numbers of intersection distributions.

TABLE IV
$\psi_{B12p,max}$ AT DIFFERENT FAULT RESISTANCES

Fault resistance R_f (Ω)	1) $\psi_{B12p,max}$	2) $\psi_{B12p,max}$	3) $\psi_{B12p,max}$	4) $\psi_{B12p,max}$
0.1	(8π/9, 11π/12]	(31π/36, 8π/9]	(7π/9, 29π/36]	(25π/36, 13π/18]
200	(5π/5, 31π/36]	(7π/9, 29π/36]	(25π/36, 13π/18]	(11π/18, 23π/36]
800	(2π/3, 25π/36]	(11π/18, 23π/36]	(7π/12, 11π/18]	(19π/36, 5π/9]

3) Different Fault Pole Types

A P-PTG fault and a PTP fault occur at f1 (the midpoint of Line1). The fault resistance is set to 0.1 Ω. Figure 14 shows the mapping relationships of Δi_{B12p} and Table V lists the values $\psi_{B12p,max}$ derived for different fault types.

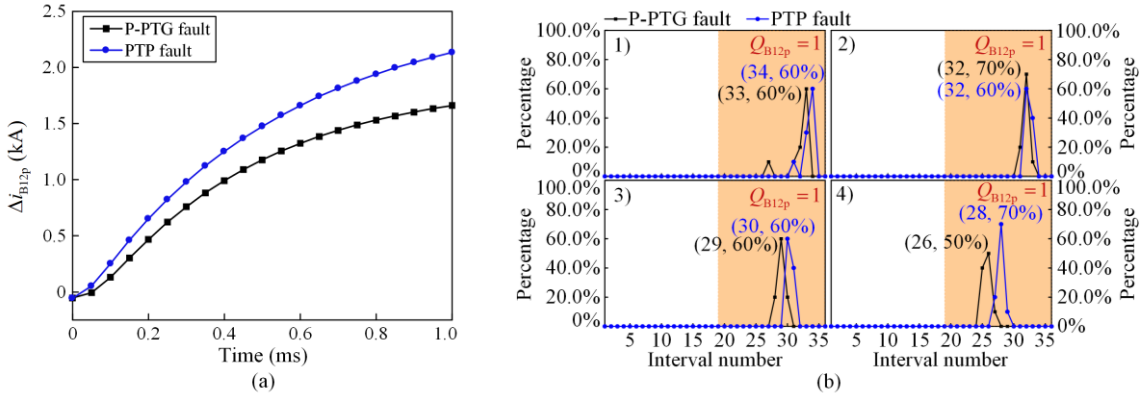

Fig. 14. Mapping relations of current waveforms at different fault pole types. (a) Waveform of transient current. (b) Interval numbers of intersection distributions.

TABLE V
$\psi_{B12p,max}$ AT DIFFERENT FAULT POLE TYPES

Fault pole type	1) $\psi_{B12p,max}$	2) $\psi_{B12p,max}$	3) $\psi_{B12p,max}$	4) $\psi_{B12p,max}$
P-PTG fault	(8π/9, 11π/12]	(31π/36, 8π/9]	(7π/9, 29π/36]	(25π/36, 13π/18]
PTP fault	(11π/12, 17π/18]	(31π/36, 8π/9]	(29π/36, 5π/6]	(3π/4, 7π/9]

From Figs. 12–14, we observe that the current coordinate mapping interval proposed in this paper can well characterize the trend of the current waveform, and then identify the fault. The above results are consistent with the theoretical analysis.

B. Performance Verification of the Protection Scheme

P-PTG faults are set at f1 (10 km, 200 km, and 390 km from B12), at f0 and f2, as well as at f01 and f21 at the beginning of Line3 and Line2, respectively. The fault resistances are set to 0.1 Ω, 200 Ω, 600 Ω and 800 Ω. The simulation duration is 2 s, with the fault occurring at 1 s and lasting for 0.5 s.

Figures 15–18 show the interval numbers of coordinate-mapped intervals based on the above fault conditions, while Tables VI–VII show the protection performance under different fault scenarios.

From Figs. 15 and 16 and Table VI, we observe that in the case of internal faults, excluding $Q=0$, both end currents of the line have the same Q value of 1 in all four data windows. The results of any data window can identify internal faults, which aligns with the theoretical analysis. It should be noted that although the interval numbers in the fourth data window are very close to the interval $Q=-1$ when the fault resistance is 800 Ω. However, according to the previous analysis: an interval number represents a coordinate mapping interval with a range of $\pi/36$, and there is some range redundancy in the coordinate mapping interval. This does not affect the fault identification accuracy. Moreover, the proposed protection identifies the fault by the ψ_{max} at both ends of the line, and $Q=0$ at one end does not affect the fault identification.

From Figs. 17 and 18 and Table VII, we observe that in the case of external metallic faults, the currents at both ends of the line have the same Q calculated within the four data windows. The presence of fault resistance disrupts the consistency of the Q value across the four data windows. The proposed segmented data window method can identify the fault with the result calculated in the first data window, which is consistent with the theoretical analysis.

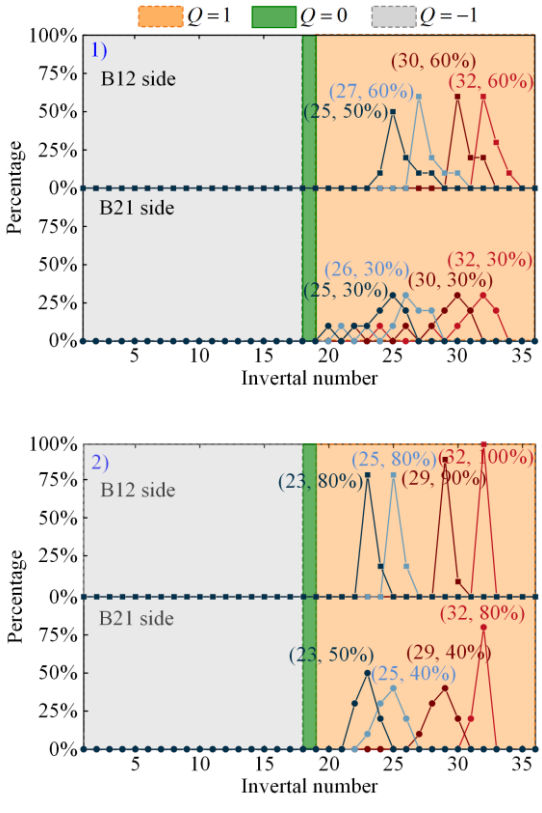

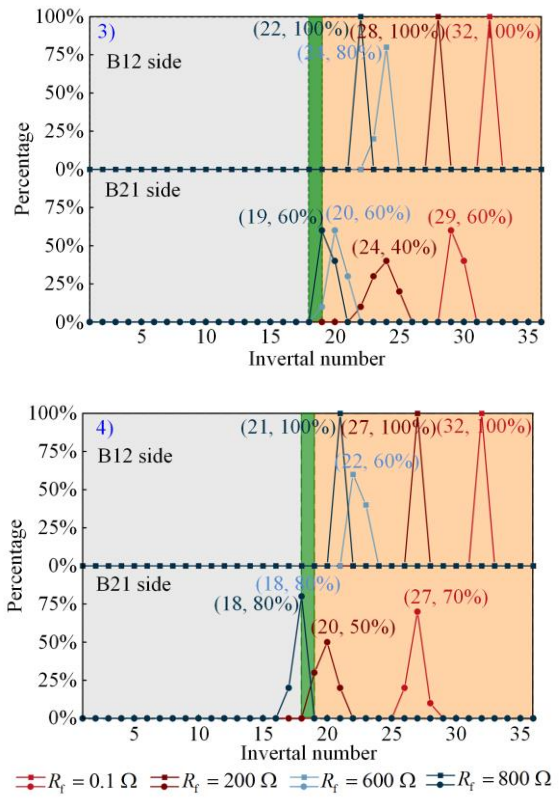

Fig. 15. The interval numbers of coordinate-mapped intervals under f1 at 10 km.

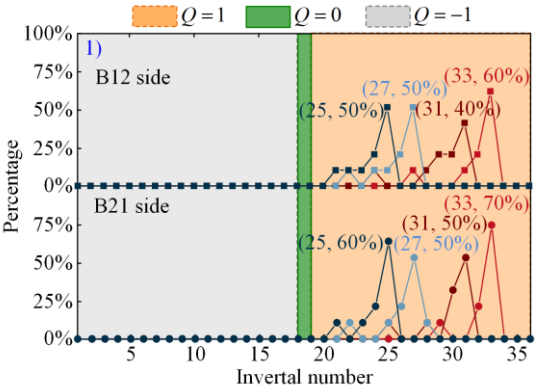

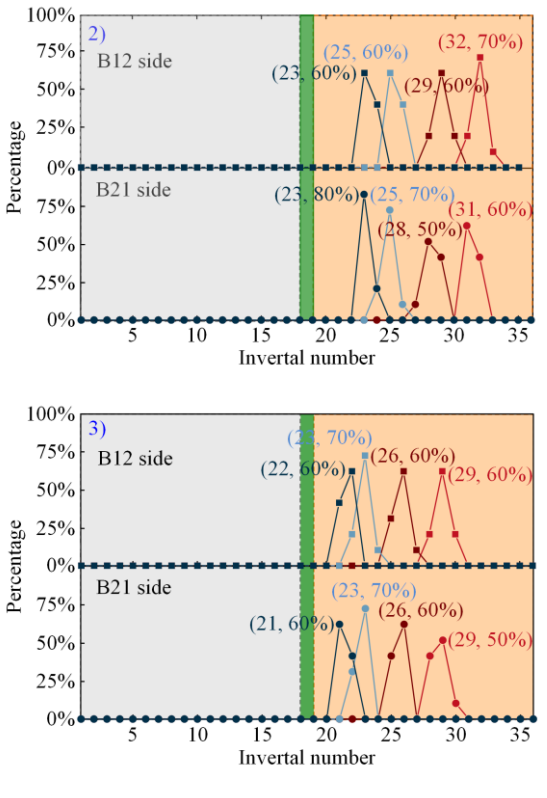

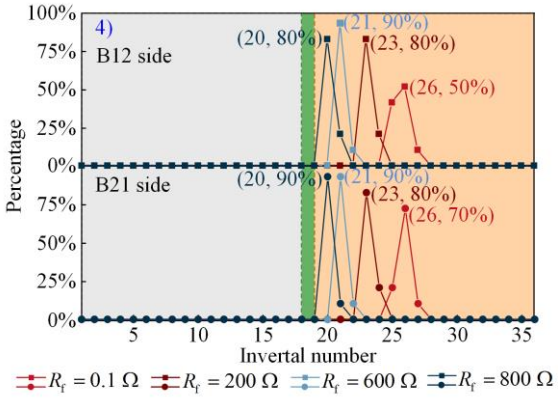

Fig. 16. The interval numbers of coordinate-mapped intervals under f1 at 200 km.

TABLE VI
SIMULATION RESULTS UNDER INTERNAL FAULTS

Fault location (km)	Fault resistance (Ω)	(Q_{B12p}, Q_{B21p}) Data window 1)	2)	3)	4)	Sum of the Q	Identification result
10	0.1	(1,1)	(1,1)	(1,1)	(1,1)	>0	Internal fault
	200	(1,1)	(1,1)	(1,1)	(1,1)		
	600	(1,1)	(1,1)	(1,1)	(1,0)		
	800	(1,1)	(1,1)	(1,0)	(1,0)		
200	0.1	(1,1)	(1,1)	(1,1)	(1,1)	>0	Internal fault
	200	(1,1)	(1,1)	(1,1)	(1,1)		
	600	(1,1)	(1,1)	(1,1)	(1,1)		
	800	(1,1)	(1,1)	(1,1)	(1,1)		
390	0.1	(1,1)	(1,1)	(1,1)	(1,1)	>0	Internal fault
	200	(1,1)	(1,1)	(1,1)	(1,1)		
	600	(1,1)	(1,1)	(1,1)	(1,1)		
	800	(1,1)	(1,1)	(1,1)	(0,1)		

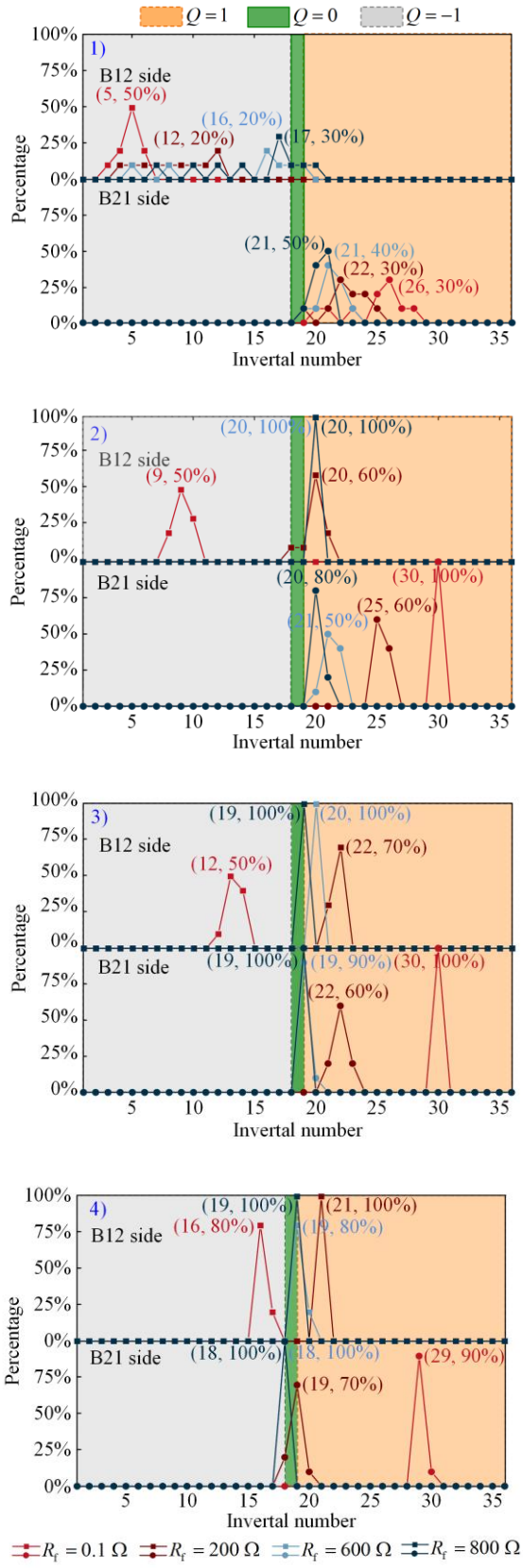

Fig. 17. The interval numbers of coordinate-mapped intervals under f0.

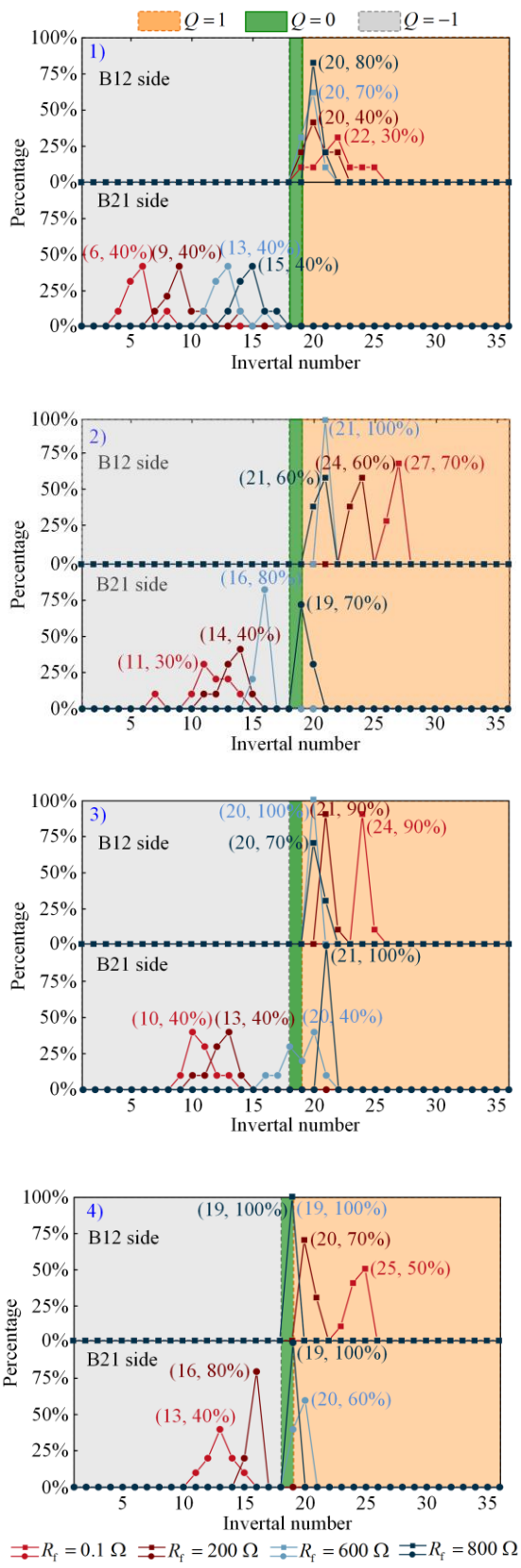

Fig. 18. The interval numbers of coordinate-mapped intervals under f21.

TABLE VII
SIMULATION RESULTS UNDER EXTERNAL FAULTS

Fault location	Fault resistance (Ω)	(Q_{B12p}, Q_{B21p}) Data window 1)	2)	3)	4)	Sum of the Q	Identification result
f0	0.1	(–1, 1)	(–1, 1)	(–1, 1)	(–1, 1)	⩽0	Backward external fault
	200	(–1, 1)	(1, 1)	(1, 1)	(1, 0)		
	600	(–1, 1)	(1, 1)	(1, 0)	(0, 0)		
	800	(–1, 1)	(1, 1)	(0, 0)	(0, 0)		
f01	0.1	(–1, 1)	(–1, 1)	(–1, 1)	(–1, 1)	⩽0	Backward external fault
	200	(–1, 1)	(–1, 1)	(–1, 1)	(–1, 1)		
	600	(–1, 1)	(–1, 1)	(–1, 1)	(0, 0)		
	800	(–1, 1)	(–1, 1)	(0, 1)	(0, 0)		
f2	0.1	(1, –1)	(1, –1)	(1, –1)	(1, –1)	⩽0	Forward external fault
	200	(1, –1)	(1, –1)	(1, 1)	(1, 1)		
	600	(1, –1)	(1, –1)	(1, 1)	(0, 1)		
	800	(1, –1)	(1, 0)	(0, 1)	(0, 0)		
f21	0.1	(1, –1)	(1, –1)	(1, –1)	(1, –1)	⩽0	Forward external fault
	200	(1, –1)	(1, –1)	(1, –1)	(1, –1)		
	600	(1, –1)	(1, –1)	(1, 1)	(0, 1)		
	800	(1, –1)	(1, 0)	(1, 1)	(0, 0)		

C. Faulty Pole Selection Verification

P-PTG fault, N-PTG fault, and PTP fault are set at f1 (200 km from B12, and $R_f = 0.1\,\Omega$). The protection performance under different fault conditions is listed in Table VIII. We observe that the proposed protection scheme can effectively identify the polarity of the fault line.

TABLE VIII
SIMULATION RESULTS AT DIFFERENT FAULT POLES

Fault location	$(Q_{B12\#}, Q_{B21\#})$	Data window 1)	2)	3)	4)	Identification result
P-PTG	(Q_{B12p}, Q_{B21p})	(1, 1)	(1, 1)	(1, 1)	(1, 1)	P-PTG fault
	(Q_{B12n}, Q_{B21n})	(1, –1)	(1, –1)	(0, 0)	(0, 0)	
N-PTG	(Q_{B12p}, Q_{B21p})	(–1, 1)	(–1, 1)	(0, 0)	(0, 0)	N-PTG fault
	(Q_{B12n}, Q_{B21n})	(1, 1)	(1, 1)	(1, 1)	(1, 1)	
PTP	(Q_{B12p}, Q_{B21p})	(1, 1)	(1, 1)	(1, 1)	(1, 1)	PTP fault
	(Q_{B12p}, Q_{B21p})	(1, 1)	(1, 1)	(1, 1)	(1, 1)	

D. Analysis of Influencing Factors

1) Influence of Fault Resistance and Distributed Capacitance Currents

Tables VI–VIII show the identification of the protection criterion considering different fault scenarios. It can be observed that the proposed scheme demonstrates robustness and sensitivity even with increasing fault resistance. Moreover, the line model adopted in this paper is a frequency-dependent parameter model, as shown in Fig. 11, i.e., the line-distributed capacitance has been considered. Therefore, the protection scheme proposed in this paper is not affected by the distribution capacitance of the line.

2) Noise Interference

Table IX shows the simulation results of the proposed protection scheme under a P-PTG fault with 800 Ω resistance and 30 dB Gaussian white noise.

TABLE IX
THE PERFORMANCE UNDER NOISE INTERFERENCE

Fault location	(Q_{B12p}, Q_{B21p}) Data window 1)	2)	3)	4)	Identification result
f0	(–1, 1)	(1, 1)	(0, 0)	(0, 0)	Backward external fault
f1 10 km	(1, 1)	(1, 1)	(1, 0)	(1, 0)	Internal fault
f1 390 km	(1, 1)	(1, 1)	(1, 1)	(0, 1)	Internal fault
f2	(1, –1)	(1, 1)	(0, 0)	(–1, 0)	Forward external fault

Simulation results show that the addition of noise does affect the waveform. The proposed protection criterion focuses on the waveform trend. This makes it less susceptible to random fluctuations and enables

reliable fault detection even at 30 dB of noise interference.

3) Impact of Fuzzy Interval

The range of the fuzzy interval is determined by k. Setting $k=2.5°$, $k=5°$ and $k=10°$ correspondingly, $\Delta\theta=k$. The previous theoretical analyzes and simulation results demonstrated that $\psi_{\max}$ generally falls in the fuzzy interval in the case of high resistance faults at the far end. Therefore, to analyze the effect of different fuzzy intervals on the protection scheme, a P-PTG fault is set to occur at f1 (390 km away from B12) and f2 with a fault resistance of 800 Ω. Figure 19 and Table X show the distribution of interval numbers and protection actions under different fuzzy intervals, respectively.

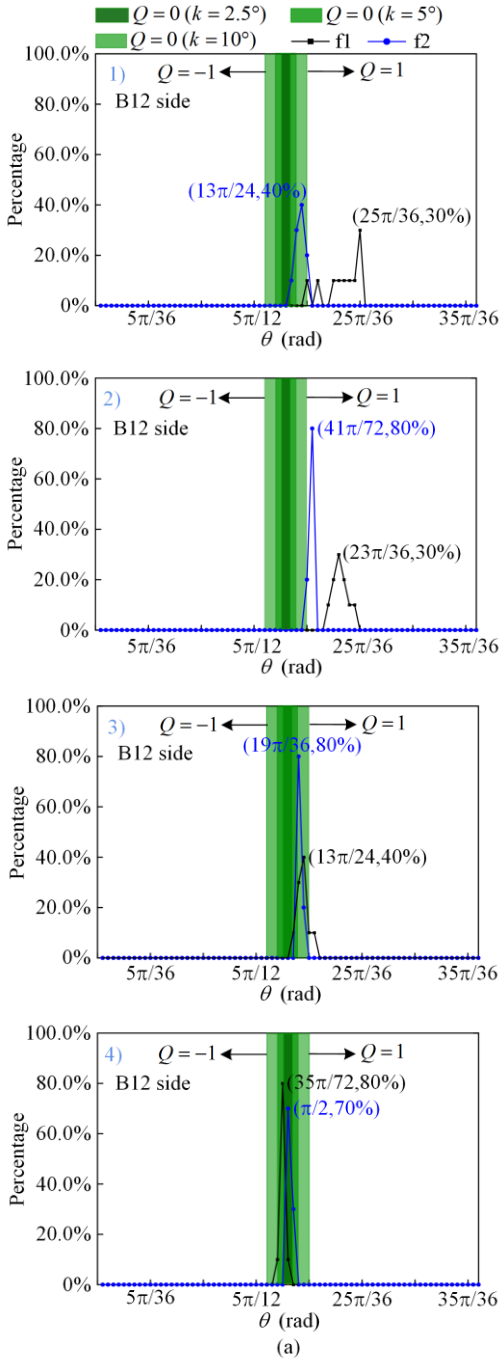

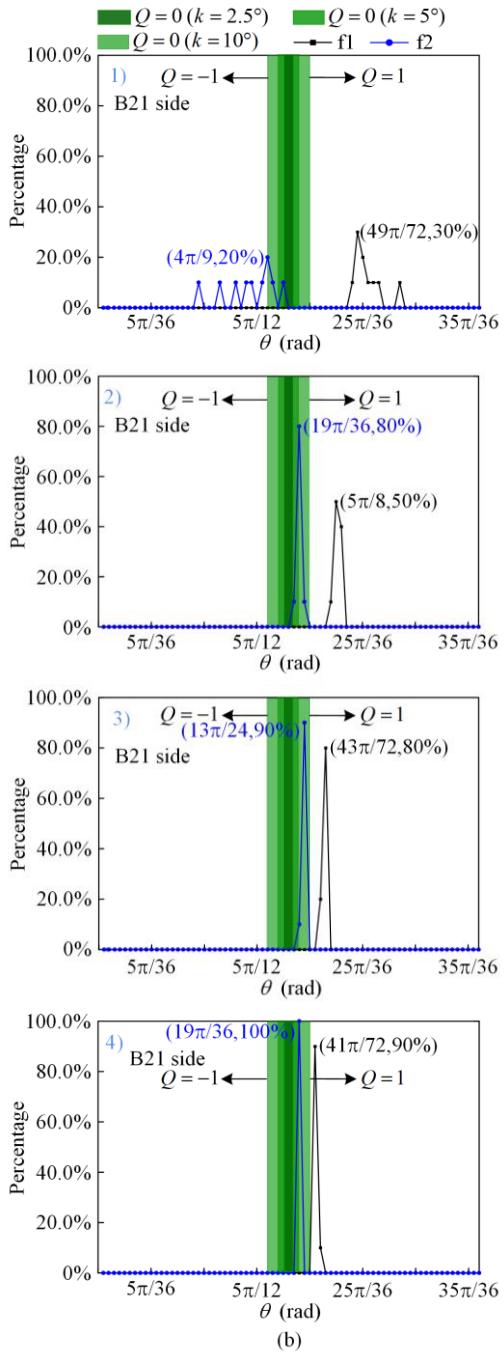

Fig. 19. Interval numbers under different fuzzy intervals. (a) B12 side. (b) B21 side.

From the simulation results, we observe that the larger k is, the smaller the range that can be recognized by the protection criterion. In the case of f2, when $k=10°$, the current coordinate mapping interval is almost always within the fuzzy interval, making it difficult to accurately identify the fault. Whereas a smaller value of k increases the sensitivity of the protection scheme to faults, it can also come at the expense of reliability. For example, in case of f1, Q on the B12 side is recognized as −1 in the fourth data window, which causes protection rejection. Therefore, to ensure the performance of the protection, $k=5°$ is a more appropriate choice.

TABLE X
THE PERFORMANCE UNDER DIFFERENT FUZZY INTERVALS

Fault location	Value of k (°)	(Q_{B12p}, Q_{B21p}) Data window				Sum of the Q
		1)	2)	3)	4)	
f1	2.5	(1, 1)	(1, 1)	(1, 1)	(–1, 1)	>0
	5	(1, 1)	(1, 1)	(1, 1)	(0, 1)	>0
	10	(1, 1)	(1, 1)	(0, 1)	(0, 1)	>0
f2	2.5	(1, –1)	(1, 1)	(1, 1)	(0, 1)	≤0
	5	(1, –1)	(1, 0)	(0, 1)	(0, 0)	≤0
	10	(0, 0)	(1, 0)	(0, 0)	(0, 0)	>0

4) Time Required to Protect the Action

The action time T_{ac} of the proposed protection is:

$$T_{ac} = T_{id} + T_{de} + T_{st} + T_{o} \tag{23}$$

where $T_{id} = 1\,\text{ms}$ is the data window time; T_{de} is the communication delay, which is 4.9 μs/km; T_{st} is the signal transmission delay calculated based on the speed of light; and $T_{o} = 0.2\,\text{ms}$ is the fixed delay for data acquisition and processing. The action time is mainly limited by communication delay and signal transmission. In the 400 km system, the proposed protection scheme achieves an action time of 4.49 ms, which satisfies the requirement for fast backup protection in MMC-HVDC systems. Moreover, the proposed protection scheme communicates only logical data after independent discrimination at both ends of the line, and does not require synchronization of data at both ends.

E. Comparison with the Existing Methods

To demonstrate the superiority of the proposed protection, a comparison is made with the existing methods from four aspects: fault resistance tolerance, noise interference, the method for determining the threshold value, and data synchronization requirements. The comparison results are shown in Table XI, where the symbol '√' represents the following criteria: fault resistance ≥ 800 Ω, noise immunity ≤ 30 dB. '/' indicates that the technical requirements are not discussed in the literature.

TABLE XI
COMPARISON RESULTS

Method	Fault resistance (Ω)	Noise Impact (dB)	Manner of setting the setting value	Data synchronisation
[14]	100	√	Calculation	Yes
[15]	100	√	Calculation	Yes
[19]	100	/	Simulation	No
[20]	400	/	Calculation	No
[22]	200	/	Simulation	No
[23]	300	40	Calculation	No
[25]	400	35	Simulation	No
The proposed scheme	800	30	Calculation	No

References [14] and [15] introduce cosine similarity and the t-test algorithm, respectively, to identify the fault region by comparing the similarity of the fault currents at both ends of the line. Protection based on similarity has higher data synchronization requirements, and data loss or anomalous data during transmission can affect the performance of the protection. To identify the fault region, references [19] and [20] use transient current and initial electrical current wave polarity, respectively. The increase in fault resistance slows down the change in fault current. This can cause the current to fall below the threshold required for the protection scheme to activate within a short timeframe, resulting in a low sensitivity of the protection to high-resistance faults. References [22] uses transient energy ratio of high-frequency and low-frequency transient energy from different outgoing lines at the converter station to construct a directional criterion. However, the range of high and low frequencies bands cannot be determined by calculation. References [23] and [25] use the difference in arrival time between forward and backward traveling waves to identify the fault region. When a high-resistance fault occurs on a long-distance line, the traveling waves severely attenuate, making it difficult to accurately detect the positive and negative traveling waves.

From Table XI, we observe that the proposed protection scheme has optimal overall performance. The threshold value used in the proposed scheme can be easily determined through calculations. Moreover, the proposed scheme does not require data synchronization, making it universally applicable.

VI. Conclusion

Existing unit protection schemes are susceptible to the influence of distributed capacitance and high fault resistance, leading to protection mis operation. Therefore, this paper proposes a unit protection scheme based on transient current coordinate mapping interval. The proposed scheme is simulated and verified in PSCAD/EMTDC, and the following conclusions are obtained.

1) The scheme exhibits high tolerance to fault resistance, maintaining accurate detection even for faults as high as 800 Ω.

2) The scheme is validated using a frequency-dependent overhead line model. The model is unaffected by distributed capacitor currents and has good interference immunity.

3) The proposed protection scheme communicates only logical data after independent identification at both ends of the line, and does not require synchronization of data at both ends.

4) A four-terminal MMC-HVDC transient simulation model is constructed in PSCAD to verify the effectiveness and advantages of the proposed protection scheme. However, due to the limitation of working conditions, the real-time simulation and verification of the proposed protection using an RTDS need to be further explored.

Acknowledgment

Not applicable.

Authors' Contributions

Yao Sun: original draft, conceptualization, formal analysis, methodology, software, writing-review & editing. Yanfang Fan: resources, supervision, writing-review & editing. Junjie Hou: supervision, writing-review & editing. Guobing Song: resources, supervision, writing-review & editing. All authors read and approved the final manuscript.

Funding

This work is supported by the Tianshan Talent Training Program (No. 2022TSYCLJ0019), the National Key R&D Program of China (No. 2021YFB1507000), the Excellent Doctoral Research and Innovation Project of Xinjiang University (No. XJU2022BS094), and the Natural Science Foundation of Xinjiang Uygur Autonomous Region Sponsored Programs (No. 2022D01C662).

Availability of Data and Materials

Please contact the corresponding author for data material request.

Declarations

Competing interests: The authors declare that they have no known competing financial interests or personal relationships that could have appeared to influence the work reported in this article.

Authors' Information

Yao Sun received her B.S. degree in electrical engineering and automation from Xinjiang University, Ürümqi, China, in 2019, where she is presently working towards her Ph.D. degree in the School of Electrical Engineering. Her current research interests include new energy grid-connection technology and power system relay protection.

Yanfang Fan received her B.S. degree in electrical engineering and automation from Xinjiang University, Ürümqi, China, in 1993, and her M.S. degree in mechanical engineering and automation from the Huazhong University of Science and Technology, Wuhan, China, in 2001. She is presently working as a professor in the School of Electrical Engineering, Xinjiang University. Her current research interests include new energy grid-connection technology and power system relay protection.

Junjie Hou received his Ph.D. degree from the School of Electrical Engineering, Xi'an Jiaotong University, Xi'an, China, in 2022. He is presently working as a teacher in the School of Electrical Engineering, Xinjiang University, Ürümqi, China. His current research interests include transmission line protection and fault location.

Guobing Song received his Ph.D. degree from the School of Electrical Engineering, Xi'an Jiaotong University, Xi'an, China, in 2005. He is presently working as a professor in the School of Electrical Engineering, the Xi'an Jiaotong University. His current research interests include transmission line fault location and protections.

References

[1] Z. Xu, "Control and fault protection of flexible DC transmission grids," in *Flexible DC Transmission System*, 2nd ed., Beijing, China: China Machine Press, 2017, pp. 190-279.

[2] R. Luo, H. Gao, and F. Peng *et al*., "An adaptive low-voltage ride-through method for virtual synchronous generators during asymmetrical grid faults, " *IEEE Transactions on Sustainable Energy*, vol. 15, no. 3, pp. 1589-1600, Jul. 2024.

[3] Y. Sun, Y. Fan, and J. Hou, "Capacitor commutation type DC circuit breaker with fault character discrimination capability," *Journal of Power Electronics*, vol. 23, pp. 1016-1027, Jan. 2023.

[4] J. Hou, G. Song, and Y. Fan, "Fault identification scheme for protection and adaptive reclosing in a hybrid multi-terminal HVDC system," *Protection and Control of Modern Power Systems*, vol. 8, no. 2, pp. 1-17, Apr. 2023.
[5] Y. Song, Y. Luo, and X. Xiong, "Loss distribution analysis and accurate calculation method for bulk-power MMC," *Protection and Control of Modern Power Systems*, vol. 8, no. 4, pp. 1-17, Oct. 2023.
[6] M. Radwan and S. P. Azad, "Protection of multi-terminal HVDC grids: a comprehensive review," *Energies*, vol. 15, no. 24, Dec. 2022.
[7] B. Li, Y. Li, and J. He *et al*., "A novel single-ended transient-voltage-based protection strategy for flexible DC grid," *IEEE Transactions on Power Delivery*, vol. 34, no. 5, pp. 1925-1937, Oct. 2019.
[8] Z. Dai, X. Liu, and Y. He *et al*., "Single-terminal quantity based line protection for ring flexible DC distribution grids," *IEEE Transactions on Power Delivery*, vol. 35, no. 1, pp. 310-323, Feb. 2020.
[9] Y. Li, L. Wu, and J. Li *et al*., "DC fault detection in MTDC systems based on transient high frequency of current," *IEEE Transactions on Power Delivery*, vol. 34, no. 3, pp. 950-962, Jun. 2019.
[10] X. Wang, S. Yang, and J. Wen, "ANN-based robust DC fault protection algorithm for MMC high-voltage direct current grids," *Institution of Engineering and Technology*, vol. 14, no. 2, pp. 199-210, Dec. 2019.
[11] B. Li, J. He, and Y. Li *et al*., "A review of the protection for the multi-terminal VSC-HVDC grid," *Protection and Control of Modern Power Systems*, vol. 4, no. 3, pp. 1-11, Jul. 2019.
[12] D. Tzelepis, A. Dysko, and G. Fusiek *et al*., "Single-ended differential protection in MTDC networks using optical sensors," *IEEE Transactions on Power Delivery*, vol. 32, no. 3, pp. 1605-1615, Jun. 2017.
[13] A. Meghwani, S. C. Srivastava, and S. Chakrabarti, "A new protection scheme for DC microgrid using line current derivative," in *Proceedings of IEEE Power Energy Society General Meeting*, Denver, USA, Jul. 2015, pp. 1-5.
[14] K. Jia, C. Wang, and T. Bi *et al*., "Transient current waveform similarity based protection for flexible DC distribution system," *IEEE Transactions on Industrial Electronics*, vol. 66, no. 12, pp. 9301-9311, Dec. 2019.
[15] K. Jia, C. Wang, and T. Bi *et al*., " Transient current correlation based protection for DC distribution System," *IEEE Transactions on Industrial Electronics*, vol. 67, no. 11, pp. 9927-9936, Nov. 2020.
[16] H. Liu, B. Li, and W Wen *et al*., "Ultra-fast current differential protection with high-sensitivity for HVDC transmission lines," *International Journal of Electrical Power & Energy Systems*, vol. 126, Mar. 2021.
[17] M. J. Perez-Molina, D. M. Larruskain, and P. Eguia Lopez *et al*., "Review of protection systems for multi-terminal high voltage direct current grids," *Renewable and Sustainable Energy Reviews*, vol. 144, Jul. 2021.
[18] V. Psaras, A. Emhemed, and G. Adam *et al*., "Review and evaluation of the state of the art of DC fault detection for HVDC grids," in *2018 53rd International Universities Power Engineering Conference*, Glasgow, UK, Sept. 2018, pp. 1-6.
[19] G. Song, X. Cai, and D. Li *et al*., "A novel pilot protection principle for VSC-HVDC cable lines based on fault component current," in *2012 Power Engineering and Automation Conference*, Wuhan, China, Sept. 2012, pp. 1-4.
[20] G. Zou, Q. Feng, and Q. Huang, *et al*., "A fast protection scheme for VSC based multi-terminal DC grid," *International Journal of Electrical Power & Energy Systems*, vol. 98, pp. 307-314, Jun. 2018.
[21] M. Jing, X. Zhao, and C. Peng, "A pilot protection scheme for flexible HVDC transmission lines based on modulus power," *International Journal of Electrical Power & Energy Systems*, vol. 137, May 2022.
[22] T. Zheng, Z. Li, and Y. Chen, "Protection scheme for a multi-terminal flexible DC grid line based on low frequency transient energy ratios of different outgoing lines at the converter station," *Power System Protection and Control*, vol. 51, no. 24, pp. 1-12, Dec. 2023. (in Chinese)
[23] L. Jiang, C. Qing, and W. Huang *et al*., "A novel directional pilot protection method for VSC-MTDC based on the initial forward and backward travelling wave head," *International Journal of Electrical Power & Energy Systems*, vol. 109, pp. 198-206, Jul. 2019.
[24] Y. Li, Y. Gong, and B. Jiang, "A novel traveling-wave-based directional protection scheme for MTDC grid with inductive DC terminal," *Electric Power Systems Research*, vol. 157, pp. 83-92, Apr. 2018.
[25] X. Yu and L. Xiao, "A DC fault protection scheme for MMC-HVDC grids using new directional criterion," *IEEE Transactions on Power Delivery*, vol. 36, no. 1, pp. 441-451, Feb. 2021.
[26] Y. Zhang, C. Wang, and Y. Yu, "A pilot protection method based on the similarity of initial current traveling wave time-frequency matrix for VSC-HVDC grids," *Electric Power Systems Research*, vol. 217, Apr. 2023.